Analytical and Bioanalytical Chemistry
https://doi.org/10.1007/s00216-018-1115-6

PAPER IN FOREFRONT

How to accurately predict solution-phase gold nanostar stability

Wenjing Xi[1] · Hoa T. Phan[1] · Amanda J. Haes[1]

Received: 26 February 2018 / Revised: 24 March 2018 / Accepted: 26 April 2018

Abstract
Unwanted nanoparticle aggregation and/or agglomeration may occur when anisotropic nanoparticles are dispersed in various solvents and matrices. While extended Derjaguin–Landau–Verwey–Overbeek (DLVO) theory has been successfully applied to predict nanoparticle stability in solution, this model fails to accurately predict the physical stability of anisotropic nanostructures; thus limiting its applicability in practice. Herein, DLVO theory was used to accurately predict gold nanostar stability in solution by investigating how the choice of the nanostar dimension considered in calculations influences the calculated attractive and repulsive interactions between nanostructures. The use of the average radius of curvature of the nanostar tips instead of the average radius as the nanostar dimension of interest increases the accuracy with which experimentally observed nanoparticle behavior can be modeled theoretically. This prediction was validated by measuring time-dependent localized surface plasmon resonance (LSPR) spectra of gold nanostars suspended in solutions with different ionic strengths. Minimum energy barriers calculated from collision theory as a function of nanoparticle concentration were utilized to make kinetic predictions. All in all, these studies suggest that choosing the appropriate gold nanostar dimension is crucial to fully understanding and accurately predicting the stability of anisotropic nanostructures such as gold nanostars; i.e., whether the nanostructures remain stable and can be used reproducibly, or whether they aggregate and exhibit inconsistent results. Thus, the present work provides a deeper understanding of internanoparticle interactions in solution and is expected to lead to more consistent and efficient analytical and bioanalytical applications of these important materials in the future.

Keywords Gold nanostars · Size · Stability · DLVO theory

Introduction

Anisotropic gold nanoparticles synthesized via seed-mediated [1, 2] and seed-less [3] as well as surfactant-based [4, 5] and surfactant-free [6, 7] synthetic methods exhibit shape- and size-tunable optical properties [8, 9] that are widely used in chemical [10], biological [11, 12], and medical sensing [13] applications. Gold nanostars exhibit large surface energies and small features (relative to spheres and larger structures) with positive and negative curvature, so flocculation and restructuring of the nanostars in solution are likely over time. Restructuring, for example, most likely occurs at regions of high surface free energy, such as at the ends of the nanostar branches (i.e., the tips) because of their small positive radii of curvature relative to other surface sites on these nanostructures [14]. This was demonstrated when the tips of gold nanostars were shown to dissolve more quickly than other parts of the nanostars in an acidic medium [15, 16]. Additionally, gold nanostar branches were shown to blunt upon irradiation by a near-infrared (NIR) laser [17]. These dynamic structural changes complicate the elucidation of structure–function relationships for these materials and can limit their shelf-life.

The reproducible use of these nanomaterials in analytical and bioanalytical applications is also limited by particle homogeneity [18], aging [19], and physical stability [20]. For instance, the ionic strength [21] and pH [22] of the solution were shown to induce nanostar aggregation, while the temperature during synthesis greatly influenced the reproducibility of the resulting plasmonic properties of the materials [23]. Localized surface plasmon resonance (LSPR) spectroscopy

Published in the topical collection *Analytical Developments in Advancing Safety in Nanotechnology* with guest editors Lisa Holland and Wenwan Zhong.

✉ Amanda J. Haes
amanda-haes@uiowa.edu

[1] Department of Chemistry, University of Iowa, 204 IATL, Iowa 52242, USA

Published online: 11 May 2018

revealed that the morphology of gold nanostars changed during storage [19]. Furthermore, the supporting electrolyte composition and concentration as well as surface functionalization with molecules such as PEG [24], PVP [25], PSS-PDD multilayers [26], and hyperbranched polymers [27] were found to influence nanostar stability. These functionalized nanostructures provide excellent examples of why nanostructure stability is important in analytical applications. For instance, fluorophore-labeled PSS-PDD multilayers were shown to stabilize gold nanostars [26], allowing more reproducible fluorescence imaging. This was attributed, in part, to the elimination of fluorophore quenching, which depends on interparticle interactions. Consequently, there are many important parameters that need to be considered in order to attain nanostars with reproducible functionality and adequate shelf-lives for desired applications.

The shelf-life and functionality of nanostructures also depend on the inherently high surface energy of these materials, as flocculation is a surface-energy-driven process [28]. Nanoparticle flocculation occurs when short-range attractive potentials exceed longer-range repulsive interactions, both of which can be modeled using DLVO theory [29–31]. This model assumes that the interaction potential between a pair of nanostructures can be estimated using the dielectric properties of the nanostructures and the medium as well as the shapes and sizes of the nanostructures. Note that the van der Waals potential between two identical nanoparticles depends on their dielectric constant. As a result [32], the attractive potential between two metallic nanoparticles at a fixed separation distance increases as the nanoparticle size decreases [28]. This causes smaller nanoparticles to more readily flocculate (i.e., exhibit worsening physical stability) than larger objects.

Because gold nanostars exhibit complex geometries involving positive, negative, and neutral curvatures, the physical stability of gold nanostars likely depends on the chemical potentials of these features. The nanostar region with the largest chemical potential (i.e., surface free energy) is likely to be the most important factor in determing stability (and thus shelf-life) of the nanostars. In the work reported in the present paper, we investigated how the ionic strength of the supporting electrolyte $NaNO_3$ impacts the optical and physical stability of gold nanostars before and after functionalization with 6-mercaptohexanoic acid (6-MHA) as a function of average particle size or radius of curvature of the nanostar tips. Those experimental results were then interpreted using collision theory and (extended) DLVO theory. We found that the solution-phase nanostar stability observed via LSPR spectroscopy can be predicted by considering the radius of curvature of the nanostar tips rather than the average nanostar size. This suggests that small changes in these areas of high chemical potential likely impact the shelf-lives and use of these increasingly popular nanostructures.

Materials and methods

Chemical reagents Gold(III) chloride trihydrate ($HAuCl_4 \cdot 3H_2O$), 4-(2-hydroxyethyl)-1-piperazine propanesulfonic acid (EPPS), and 6-mercaptohexanoic acid (6-MHA) were purchased from Sigma–Aldrich (St. Louis, MO, USA). Sodium hydroxide (NaOH), sodium nitrate ($NaNO_3$), and ethanol were purchased from Fisher Scientific (Loughborough, UK). Water (18.2 MΩ cm^{-1}) used throughout this study was obtained from a Barnstead Nanopure System (Dubuque, IA, USA). All glassware were cleaned using aqua regia (3:1 HCl/HNO_3) and rinsed with water before drying them in the oven.

Gold nanostar synthesis and functionalization Gold nanostars were synthesized according to slightly modified literature protocols [33, 34]. Briefly, the pH of a 50 mM EPPS solution was adjusted to 7.45 using 1 M NaOH. $HAuCl_4$ (200 μL, 20 mM) was then added to 20 mL EPPS and incubated for 2 h. Next, an additional 50 μL of 20 mM $HAuCl_4$ was added to the solution to promote nanostar growth. This solution was stirred for 60 min at 35°C, centrifuged (40 min, 2000×*g*) three times, and dispersed in 1 mM EPPS until use. The stock Au nanostar concentration was 0.48 nM, as estimated using a previously published extinction coefficient ($\varepsilon = 2.08 \times 10^9$ M^{-1} cm^{-1}) [35]. Gold nanostar functionalization with 6-MHA was performed exactly according to our previously published protocol [34].

Transmission electron microscopy (TEM) Gold nanostars were characterized using a TEM (JEM-1230, JEOL, Tokyo, Japan) equipped with a Gatan (Pleasanton, CA, USA) CCD camera and an accelerating voltage of 120 keV. Samples were prepared by first diluting the nanoparticle solution by 50% with ethanol. This solution was pipetted onto 400-mesh copper grids coated with a thin film of formvar and carbon (Ted Pella, Redding, CA, USA). TEM images were analyzed (Image Pro Analyzer or Image J) to estimate the average overall (ferret) radius before (33.0 ± 8.6 nm, $N = 163$) and after (24.8 ± 5.0 nm, $N = 149$) functionalization, as well as the radius of curvature of the tips (before functionalization: 4.4 ± 0.8 nm, $N = 213$; after: 4.5 ± 0.5 nm, $N = 205$), where N is the total number of measurements collected, and the average ± standard deviation of these are reported.

Extinction spectroscopy LSPR spectra were collected using disposable methacrylate cuvettes (pathlength = 1 cm) and an ultraviolet-visible (UV-vis) spectrometer (i-trometer, B&W Tek, Newark, DE, USA). Samples were prepared by diluting the stock gold nanostars in water to a final nanostar concentration of ~0.3 nM. Next, 1 M $NaNO_3$ was added slowly to the nanostar solutions such that the final electrolyte concentration ranged from 0 to 50 mM. The final EPPS concentration in all

samples was 0.6 mM. For each sample, a LSPR spectrum (integration time = 36 ms, average = 50 scans) was collected every 15 s for 1 h, with a lag time of 25 s. Spectral changes were evaluated by integrating the spectral regions 950–1050 nm and 520–570 nm and determining the relative changes in these (in %) vs. initial integrals. This permitted the assessment of gold nanostar stability before and after 6-MHA functionalization in terms of aggregation. Finally, the extinction maximum wavelength (λ_{max}) was estimated from the zero-point crossing of the first derivative of each LSPR spectrum.

Zeta potential Nanoparticle surface potentials were quantified from their electrophoretic mobilities at 25 °C using a Malvern Zetasizer (Worcestershire, UK). Mobilities were measured after incubation in 0–50 mM $NaNO_3$ (calculated ionic strengths = 0.15–50.15 mM, respectively). Both the residual EPPS and added electrolyte concentrations were assumed to contribute to these ionic strengths. All solutions were vortexed for 10 s and then incubated at room temperature for 1 h prior to electrophoretic mobility measurements. The zeta potential was calculated using Henry's equation, measured mobilities, and calculated ionic strengths [36]. EPPS-stabilized and 6-MHA-functionalized nanostars exhibited zeta potentials of -41.6 ± 2.9 and -32.0 ± 1.9 mV, respectively. These values represent averages of measurements obtained at all the ionic strengths used in this study.

DLVO and collision theory calculations Nanoparticle stability depends on the concentration of as well as the number of collisions between nanostructures in a given period of time. We used collision theory to estimate stability; this assumes that the minimum energy required for particles to remain physically stable and suspended in solution must exceed their kinetic energy from Brownian motion [37]. As such, the total number of collisions (z) between two particles was estimated as follows:

$$z = 4\pi r^2 \langle v \rangle N \cdot t, \tag{1}$$

where r is the nanoparticle radius (the ferret radius or the radius of curvature of the tips), N is the number of nanoparticles, and t is the time period considered. The collision rate is equal to $4\pi r^2 \langle v \rangle N$, and the root mean square speed $\langle v \rangle$ of Brownian motion can be calculated as follows:

$$\langle v \rangle = \left(\frac{8kT}{\pi \mu} \right)^{0.5}, \tag{2}$$

where k is the Boltzmann constant, T is the temperature, and μ is the reduced mass of the two objects.

DLVO theory assumes that all objects exhibit both attractive and repulsive interactions via van der Waals and electrostatic forces, respectively. For two objects with identical sizes (r), the van der Waals interaction potential (Φ_{VDW}) is calculated as follows:

$$\Phi_{VDW}(s) = \frac{V_{vdw}}{k_B T} = -\frac{A}{6}\left[\frac{2r^2}{s^2 + 4rs} + \frac{2r^2}{s^2 + 4rs + 4r^2} + \ln\left(\frac{s^2 + 4rs^2}{s^2 + 4rs + 4r^2} \right) \right], \tag{3}$$

where A is the size-dependent Hamaker constant and s is the separation distances [37, 38]. The electrostatic interaction potential (Φ_{EL}) between two objects depends on the inverse Debye length (κ) and exhibits two limits [39] first understood by Derjaguin in 1937 [30] including when κr > 5 (double layer thickness is small vs. particle radius),

$$\Phi_{EL}(s) = \frac{V_{ele}}{k_B T} = \frac{2\pi \varepsilon_0 \varepsilon {\psi_0}^2 r}{k_B T} \ln(1 + e^{-\kappa s}) \tag{4}$$

and when κr < 5 (double layer thickness is large vs. particle radius) and

$$\Phi_{EL}(s) = \frac{V_{ele}}{k_B T} = \frac{4\pi \varepsilon_0 \varepsilon Y^2 r^2 k_B T}{e^2} \frac{e^{-\kappa s}}{s + 2r} \tag{5}$$

where $Y = \frac{8\tanh\left(\frac{e\psi_0}{4k_B T}\right)}{1 + \left[1 - \frac{2\kappa r + 1}{(\kappa r + 1)^2} + tanh^2\left(\frac{e\psi_0}{4k_B T}\right)\right]^{1/2}}$; $\psi_0 = \xi\left(1 + \frac{1}{\kappa r}\right) \cdot \exp(1)$, $\kappa^{-1} = \left(\sqrt{\frac{2e^2 N_A I}{\varepsilon \varepsilon_0 k_B T}} \right)^{-1}$, ψ_0 is the surface potential, ξ is zeta potential, e is elementary charge, ε is the relative permittivity of water (78.54), ε_0 is the electric permittivity of free space, R is the gas constant, I is ionic strength (0.15–50.15 mM), and N_A is Avogadro's number.

Stability calculations for nanostructures functionalized with 6-MHA also include osmotic (Φ_{osm}) and elastic (Φ_{elas}) interaction potentials (i.e., extended DLVO). These short-range repulsive contributions depend on monolayer thickness (t) and separation distance, s [37, 40]. When the separation distance is larger than twice the effective monolayer thickness ($s > 2t$), $\Phi_{osm}(s) = 0$. When $t \leq s \leq 2t$,

$$\frac{\Phi_{osm}(s)}{k_B T} = \frac{4\pi r N_A}{\upsilon_1} {\phi_P}^2 \left(\frac{1}{2} - \chi \right) \left(t - \frac{s}{2} \right)^2 \tag{6}$$

can be used, where υ_1 is the molar volume of the solvent, χ is the Flory–Huggins interaction parameter (0.45 for a well-ordered monolayer) [41], and ϕ_P is the volume fraction of the ligand. When the separation distance is less than the effective monolayer thickness ($s < t$), ligand interactions between the nanoparticle pair cause elastic deformations and ligand tail compression [40, 41]. As a result, $\Phi_{osm}(s)$ and $\Phi_{elas}(s)$

contribute to the total interaction potential between a pair of objects and are calculated as follows:

$$\frac{\Phi_{\mathrm{osm}}(s)}{k_{\mathrm{B}}T} = \frac{4\pi r N_{\mathrm{A}}}{\upsilon_1}\phi_P{}^2\left(\frac{1}{2}-\chi\right)\left[t^2\left(\frac{s}{2t}-\frac{1}{4}-\ln\left(\frac{s}{t}\right)\right)\right] \quad (7)$$

$$\frac{\Phi_{elas}(s)}{k_BT} = \left(\frac{2\pi r N_A}{M_W}\phi_P t^2 \rho_d\right)\left(\left(\frac{s}{t}\right)\ln\left(\frac{s}{t}\left(\frac{3-\frac{s}{t}}{2}\right)^2\right)\right) - 6\ln\left(\frac{3-\frac{s}{t}}{2}\right) + 3\left(1-\frac{s}{t}\right) \quad (8)$$

where M_W (148.22 g/mol) and ρ_d (4.581×10^{14}) are the molecular weight and density of the (pure) ligand, respectively.

The total interaction potential between a pair of nanostructures is the sum of all relevant contributions ($\Phi_{\mathrm{total}}(s) = \Phi_{\mathrm{vdw}}(s) + \Phi_{\mathrm{EL}}(s) + \Phi_{\mathrm{osm}}(s) + \Phi_{elas}(s)$). The energy barriers ($V_{\mathrm{max}}$) required to determine solution-phase nanoparticle stability were estimated from the total interaction potential (Φ_{total}) and then plotted as a function of ionic strength. Nanostructures were considered to be stably suspended in solution when V_{max} was greater than the kinetic energy calculated using collision theory.

Results and discussion

Gold nanostar functionalization and characterization When nanoparticles such as gold nanostars are used in applications, the materials are typically functionalized and/or dispersed in buffer [42]. Thus, it is important to understand how functionalization and buffer composition influence the physical stability of gold nanostars. For instance, the size of a nanostructure governs its electrooptical properties, stability in solution, and how it interacts with/influences matter [28, 43]. In the present work, gold nanostars synthesized via EPPS reduction [33] were used to explore how functionalization and ionic strength impact the size, structure, surface potential, and optical stability (and hence the physical stability) of the resulting materials. 6-MHA was selected for functionalization as it forms self-assembled monolayers (SAMs) on gold [34] and contains a terminal carboxylic acid group that is deprotonated in solutions when pH is above 5.4–6.3 [44]. As a result, a repulsive steric barrier (i.e., from elastic and osmotic potentials) is present at the surface of functionalized nanostars in physiologically relevant (pH) solutions.

Representative TEM images of gold nanostars before and after functionalization are shown in Fig. 1a and b. Each nanostructure contains a core and three to seven branches, meaning that each nanostructure is star-shaped. Because of the complex shape of each nanostar, size can be quantified in multiple ways, including ferret radius, branch length, core size, and radius of curvature of the tips. The largest (ferret radius) and smallest (radius of curvature of the tips) dimensions are the most straightforward and accurate dimensions to quantify. A summary of these gold nanostar dimensions before and after functionalization with 6-MHA is provided in Fig. 1c and d. Before functionalization, the ferret radius of the nanostars was 33.0 ± 8.6 nm. Upon functionalization with 6-MHA, this value decreased to 24.8 ± 5.0 nm. This decrease in size is similar to what occurs to gold nanostructures upon thiolation [45]. The radius of curvature of the tips did not, however, change significantly upon functionalization (4.4 ± 0.8 nm vs. 4.5 ± 0.5 nm, respectively).

Along with slight structural changes, the surface potential of the nanostructures changed from −41.6 to −32.0 mV at ~pH 7. Surface potential depends on double-layer effects at

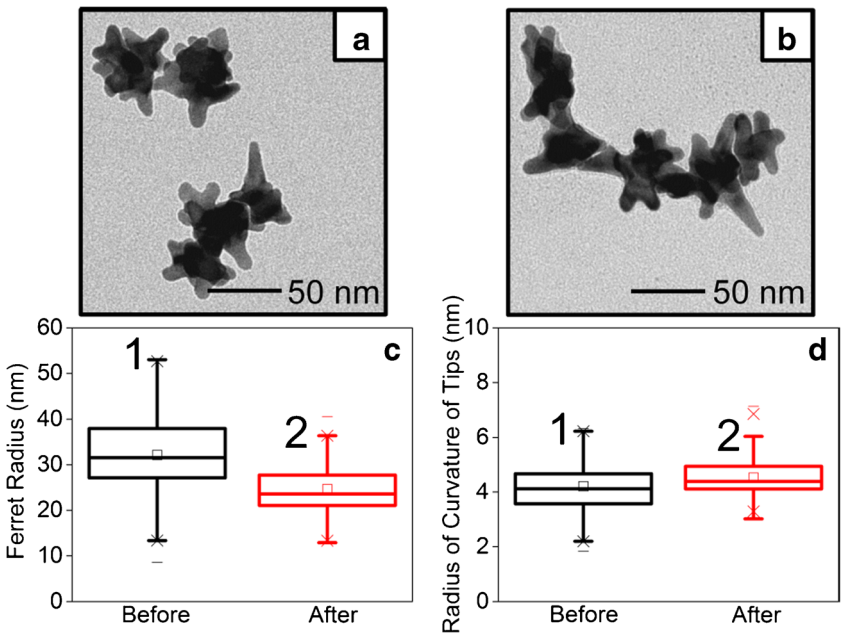

Fig. 1 **a–d** TEM analysis of gold nanostars **a** before and **b** after functionalization with 6-MHA, and the size distribution of the nanostars as functions of **c** the ferret radius and **d** the radius of curvature of the nanostar tips before (*1*; 33.0 ± 8.6 nm, $N = 163$ and 4.4 ± 0.8 nm, $N = 213$) and after (*2*; 24.8 ± 5.0 nm, $N = 149$ and 4.5 ± 0.5 nm, $N = 205$) 6-MHA functionalization

the nanoparticle surface as well as the charge on terminal functional groups of the SAM. These data suggest that the electrostatic double layer of ions from solution was larger on unfunctionalized than on functionalized nanostructures. This change in surface chemistry was also observedin LSPR analysis. Before functionalization, the λ_{max} of the nanostars was centered at 714.4 nm (Fig. 2a-1), consistent with previously reported gold nanostar optical properties [33]. Upon functionalization, this value red-shifted 11.9 nm to 726.3 nm (Fig. 2a-2). In addition, the LSPR band shape broadened, which is consistent with slight electromagnetic coupling between nanostructures. Despite this, the nanostructures remained suspended in solution and could therefore be used to estimate the effective refractive index and effective thickness of the 6-MHA monolayer.

The change in λ_{max} following functionalization can be used to estimate the effective monolayer thickness (t) and refractive index of the monolayer because the LSPR is sensitive to local refractive index [46]. SAM thickness and refractive index sensitivity (m) of the gold nanostars were calculated using the following equation [47, 48]:

$$\Delta\lambda_{max} = m\Delta n\left(1-e^{-\frac{2t}{l_d}}\right), \quad (9)$$

where Δn is the refractive index difference between the SAM and water (1.33) and l_d is the 1/e electromagnetic field decay length. The refractive index sensitivity of the gold nanostars was estimated by systematically changing the bulk refractive index of the unfunctionalized gold nanostars in solution through the introduction of 0–80% (w/v) sucrose [49]. This resulted in a refractive index sensitivity of 416 nm/refractive index unit (RIU) for electrostatically stabilized nanostars (Fig. 2b-1). After functionalization, this value decreased to 369 nm/RIU, as shown in Fig. 2b-2. The 1/e decay length was ~4 nm, which is reasonable assuming that each branch can be treated as a nanorod [34]. The effective refractive index of the SAM was estimated as 1.43_7 from the crossing point of these lines [50]. Using these values and Eq. 9, an effective SAM thickness of 0.6 nm was estimated.

Experimental evaluation of gold nanostar stability After evaluating the structure, surface potential, and surface chemistry of the nanostars, physical stability was assessed using LSPR spectroscopy. Most ions in solution exhibit weak to no affinity for gold and impact the physical stability of gold nanostars by influencing the ionic strength of the solution as well as the double-layer composition and thickness [51, 52]. Nitrate, a good electrolyte for this purpose as it exhibits minimal affinity for gold, was used in this work to adjust the ionic strength of the solution from 0.15 to 50.5 mM. Gold nanostar concentration was maintained at ~0.3 nM so that the number of collisions between nanostructures was

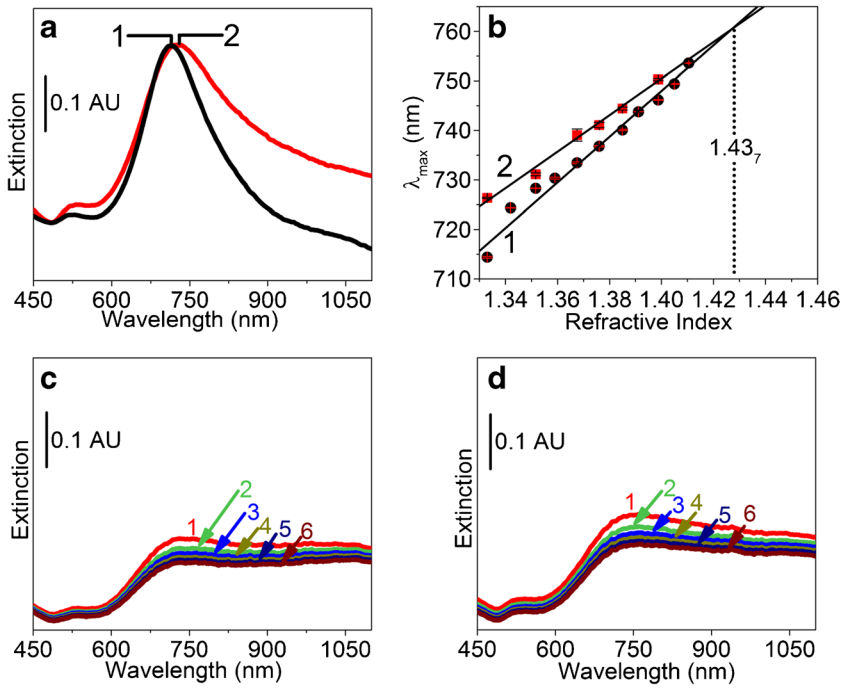

Fig. 2 **a–d** Plasmonic characterization of gold nanostars. **a** LSPR spectra ($\lambda_{max,1}$ = 714.4 nm, $\lambda_{max,2}$ = 726.3 nm, $\Delta\lambda_{max}$ = 11.9 nm) of the nanostars and **b** refractive index sensitivity of the nanostars to 0–80% (w/v) sucrose before (*1*) and after (*2*) functionalization with 6-MHA. The linear refractive index sensitivities before and after 6-MHA functionalization were 461 and 369 nm/RIU, respectively. The intersection of these lines yields the refractive index of 6-MHA on the nanostars: 1.43_7. Representative LSPR spectra of nanostars before (**c**) and after (**d**) 6-MHA functionalization are presented and were obtained after the nanostars were immersed in 50 mM $NaNO_3$ for (*1*) 10, (*2*) 20, (*3*) 30, (*4*) 40, (*5*) 50, or (*6*) 60 min

approximately constant on average as estimated using collision theory (Eqs. 1–2). While the ionic strength can slightly impact Brownian motion, this effect was assumed to be minimal. LSPR spectra for gold nanostars before and after functionalization were collected continuously for 1 h under identical conditions.

Figure 2c and d show representative time-dependent LSPR spectra for gold nanostars incubated in 50 mM $NaNO_3$ before and after 6-MHA functionalization, respectively. Similar trends are apparent for both samples. First, the λ_{max} value red-shifts with time, consistent with an increase in local refractive index caused by decreasing interparticle distances and/or cluster formation [53]. Second, the extinction magnitude at the λ_{max} decreases with time because of plasmon dampening that occurs upon nanostar aggregation. Finally, the LSPR spectra broaden significantly at longer wavelengths for the unfunctionalized gold nanostars while spectra from functionalized materials do not change. This spectral change is once again consistent with increased short-range interparticle interactions associated with cluster formation. All of these trends are time dependent, suggesting that gold nanostars with and without SAM functionalization undergo increasingly significant nanoparticle–nanoparticle interactions over time in solution at this ionic strength.

To quantify these time-dependent variations, the λ_{max} and relative integrated spectral area near 1000 nm are plotted in Fig. 3. Differences in flocculation (i.e., both agglomeration and aggregation) are reported as relative changes in integrated area ($(t_i - t_0)/t_0$, %) that were calculated from LSPR spectra [54]. Once again, interesting trends are apparent. First, the λ_{max} increases three times faster when nanostars are functionalized than when the structures are electrostatically stabilized. Second, relative changes in the integrated area for gold nanostars stabilized by SAMs reveal similar time-dependent changes in λ_{max}. The electrostatically stabilized structures, however, show more complex behavior: the value initially increases rapidly (~2 times more quickly than for the SAM-stabilized nanostars), suggesting rapid electromagnetic coupling between nanostructures before undergoing a slow decay. This behavior is consistent with the irreversible formation of clusters that subsequently settle out of solution via sedimentation. In contrast, the SAM-stabilized structures couple electromagnetically but do not form stable or large aggregates.

To closely investigate the temporal responses of these interactions, we obtained time-dependent LSPR spectra of gold nanostars with and without SAM functionalization that were incubated in 0–50 mM $NaNO_3$ for 1 h. As shown in Fig. 3a and c, the λ_{max} values of the electrostatically and 6-MHA-stabilized gold nanostars in 0–30 mM $NaNO_3$ did not change significantly during this time period. Both the electrostatically-stabilized and 6-MHA-stabilized nanostars in 30 mM $NaNO_3$, however, showed evidence of electromagnetic instability (i.e., agglomeration and/or aggregation) through shifts in λ_{max} and changes in relative integrated area. The relative integrated area near 1000 nm was more sensitive to flocculation than changes in λ_{max}. As shown in Fig. 3b, evidence of gold nanostar flocculation caused by increasing ionic strength was observed at $NaNO_3$ concentrations greater than 20 mM. In 25–30 mM $NaNO_3$, the integrated area near 1000 nm increased by ~35% over the course of an hour, whereas rapid increases in integrated areas by ~75 and 115% were observed within 5 min in 40 mM and 50 mM $NaNO_3$, respectively. After 5 min, the integrated area decreased

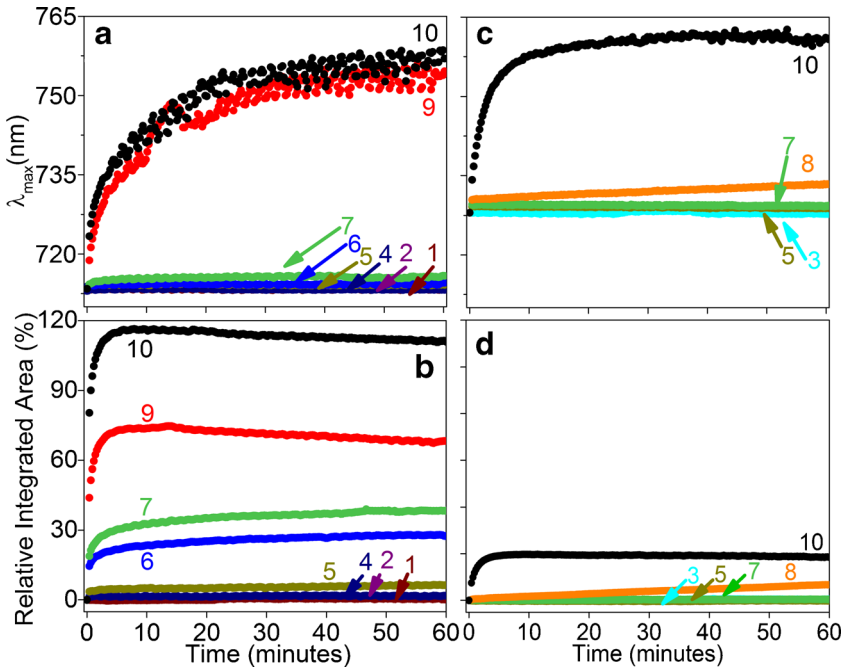

Fig. 3 **a–d** Time-dependent plasmonic responses of gold nanostars before (**a** and **b**) and after (**c** and **d**) 6-MHA functionalization in the presence of (*1*) 0, (*2*) 5, (*3*) 10, (*4*) 15, (*5*) 20, (*6*) 25, (*7*) 30, (*8*) 35, (*9*) 40, or (*10*) 50 mM $NaNO_3$. The changes in λ_{max} (**a** and **c**) and the changes in the relative integrated areas (%) from 950 - 1050 nm to 520–570 nm (**b** and **d**) are presented for gold nanostars before and after 6-MHA functionalization, respectively

slightly, consistent with sedimentation of clusters and/or plasmon dampening.

In contrast, the SAM-functionalized nanostructures did not exhibit evidence of large changes in electromagnetic coupling due to aggregation and/or sedimentation until 50 mM $NaNO_3$ was used (Fig. 3d). Only slight changes in electromagnetic coupling between nanostars were inferred when the $NaNO_3$ concentration was less than 40 mM (redshift <2 nm in the LSPR maximum wavelength and change of < 5% in the relative integrated area). As the ionic strength increased further, the λ_{max} increased by ~30 nm and the relative integrated area near 1000 nm increased rapidly by ~20% (similar to unfunctionalized nanostructures). These trends at the highest ionic strength are consistent with previously observed variations in the plasmonic changes of solution-phase gold nanostructures that arise from electromagnetic coupling and nanoparticle instabilities and cluster formation. Importantly, although the overall size [55], branch length [35], number of branches [46], and radius of curvature of nanostar tips [14] have previously been shown to influence the optical properties of similar nanostructures, little or no insight into these effects was provided by those studies.

Predicting gold nanostar stability as a function of dimension

Gold nanostar stability depends on both the energetics associated with collisions as well as the number of collisions that occur between nanostructures over a period of time. In an effort to develop a model that accurately predicts the experimentally observed nanostar stability, we employed both collision theory and DLVO modeling. Collision theory estimates the collision frequency between objects and the kinetic energies of objects from Brownian motion [37]. In this study, durations of 24 h and one week were selected to mimic sample handling and storage conditions [56]. For example, 2.2×10^7 collisions between primary nanoparticles is predicted to occur in a ~0.3 nM gold nanostar solution at 298 K over the course of one week. Assuming a Boltzmann distribution, the probability ($e^{-V_{max}/k_B T}$) that two colliding nanoparticles will overcome this energy barrier and aggregate is less than 1/(number of collisions per week). Importantly, collision theory overestimates collision frequency once clusters have formed, so results obtained using collision theory represent a worst-case scenario for stability predictions. Thus, gold nanostars must possess a minimum energy of ~16–17/$k_B T$ to remain stable in solution for one week. This value is independent of nanoparticle functionalization.

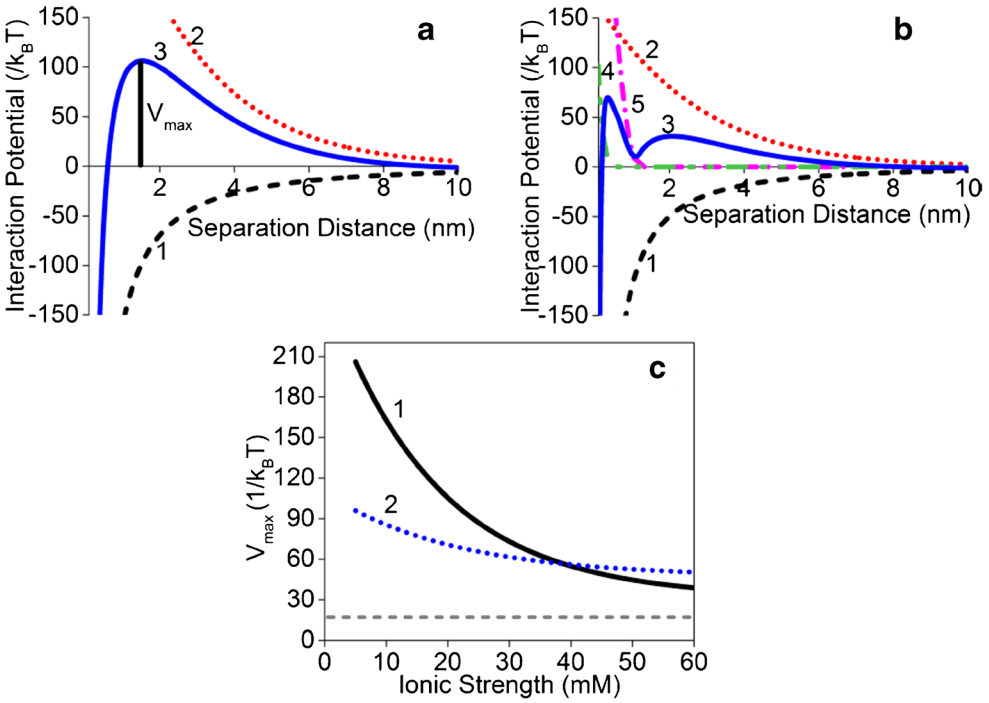

Fig. 4 **a–c** Predictions from DLVO and xDLVO theory of the interaction potential between a pair of gold nanostars as a function of nanostar size, as defined using the ferret radius, before (**a**) and after (**b**) functionalization with 6-MHA. Interaction potentials are shown as functions of the (*1*) van der Waals, (*2*) electrostatic, (*3*) total, (*4*) elastic, and (*5*) osmotic potentials. The following experimental values were used for modeling: **a** radius = 33.0 nm, Hamaker constant = 2.98×10^{-19} J, zeta potential = −41.6 mV; **b** radius = 24.8 nm, Hamaker constant = 3.10×10^{-19} J, zeta potential = −32.0 mV; ionic strength = 20 mM, molecular weight of ligand = 148.22 g/mol, density of pure ligand = 1.087 g/cm^3, SAM packing density = 4.58×10^{14}, and SAM thickness = 0.6 nm. **c** Maximum potential barrier (V_{max}) as a function of ionic strength for nanostars before (*1*) and after (*2*) functionalization. The *dashed gray line* represents the interaction potential that must be overcome to prevent aggregation by 0.3 nM nanostars stored at room temperature for one week (as estimated using collision theory)

(Extended) DLVO theory has been used in conjunction with the results from collision theory as DLVO modeling is widely applied to predict nanomaterial stability as a function of interaction pair potential [28, 37, 57, 58]. Here, we consider the impacts of both nanoparticle dimensionality (size) and functionalization. Dimensionality is an important parameter when applying this model as both van der Waals and electrostatic interactions exhibit size dependence, and extended DLVO incorporates both elastic and osmotic interaction potentials for SAM-functionalized nanostructures (these potentials are zero for unfunctionalized materials [37] as the volume fractions of the ligands are zero in Eqs. 8 and 7, respectively, which reduces these potentials to zero). When applying DLVO theory to the nanostars used in this study, the surface potential and the surface ligand densities/thicknesses were assumed to be uniform; experimental values for these parameters can be estimated using zeta potential and LSPR spectroscopy, respectively (vide supra).

When investigating how nanostar size impacts the solution-phase stability of nanostars, dimensionality can be characterized in terms of ferret radius, branch length, core size, or tip size (i.e., radius of curvature). We used the largest (ferret radius) and smallest (radius of curvature of the tips) dimensions of the nanostars considered in this study to evaluate the impact of "size" on the experimentally observed and predicted nanostructure stabilities. Interaction pair potentials for gold nanostars before (Fig. 4a) and after (Fig. 4b) 6-MHA functionalization were compared using Eqs. 3–8. The ferret radius was first used in DLVO modeling as the gold nanostar "size". Because the ferret radius decreased from 33.0 to 24.8 nm upon functionalization, previously determined size-dependent Hamaker constants of 2.98 and 3.10×10^{-19} J were used, respectively [37]. The difference between these values influences the predicted van der Waals potential between two nanostructures. Repulsive interactions are influenced by variations in electrostatic potential (−41.6 and −32.0 mV, respectively) and by the presence/absence of the SAM.

The individual contributions to the total interaction potential in a 20 mM ionic strength solution are shown for nanostars without and with 6-MHA functionalization in Fig. 4a and b, respectively. While there are clearly differences in the individual contributions before and after functionalization, the shapes of the total interaction pair potentials are consistent with previous DLVO and extended DLVO calculations for spherical particles [37]. In addition, the maximum energy barrier (V_{max})

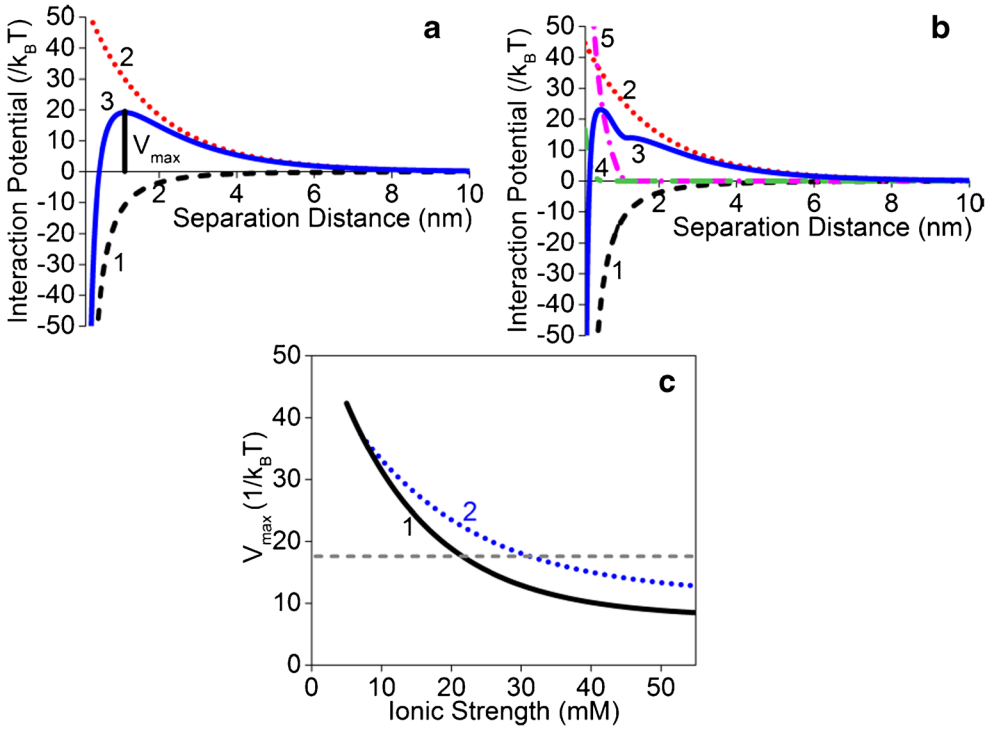

Fig. 5 **a–c** Predictions from DLVO and xDLVO theory of the interaction potential between a pair of gold nanostars as a function of nanostar size, as defined using the radius of curvature of the tips before (**a**) and after (**b**) functionalization with 6-MHA. Interaction potentials are shown as functions of the (*1*) van der Waals, (*2*) electrostatic, (*3*) total, (*4*) elastic, and (*5*) osmotic potentials. The following experimental values were used for modeling: **a** radius = 4.4 nm, Hamaker constant = 3.85×10^{-19} J, zeta potential = −41.6 mV; **b** radius = 4.5 nm, Hamaker constant = 3.85×10^{-19} J, zeta potential = −32.0 mV; ionic strength = 20 mM, molecular weight of ligand = 148.22 g/mol, density of pure ligand = 1.087 g/cm^3, SAM packing density = 4.58×10^{14}, and SAM thickness = 0.6 nm. **c** Maximum potential barrier (V_{max}) as a function of ionic strength for nanostars before (*1*) and after (*2*) functionalization. The *dashed gray line* represents the interaction potential that must be overcome to prevent aggregation by 0.3 nM nanostars stored at room temperature for 1 week (as estimated using collision theory)

decreases following functionalization from ~100/k_BT to ~60/k_BT. Similar calculations were also performed for ionic strengths ranging from 0.5 to 50.5 mM so that the trend in the theoretical V_{max} with ionic strength could be evaluated for the electrostatically and SAM-stabilized nanostructures. These trends are shown in Fig. 4c. V_{max} decreases for the nanostructures as ionic strength increases because the electrostatic double layer becomes more compressed, which lowers the electrostatic pair potential. In addition, the SAM provides additional stability when ionic strength exceeds ~38 mM. These general predictions are reasonable but inconsistent with our experimental observations of solution-phase stability of the nanostars from LSPR measurements. Furthermore, collision theory suggests that any energy barrier in excess of ~17/k_BT should result in thermodynamically stable nanostructures for one week, which implies that the ferret radius is not the dimension that governs the solution-phase stability of gold nanostars.

To improve DLVO predictions, similar modeling was performed using the radius of curvature of the nanostar tips instead of the ferret radius. The results are shown in Fig. 5a and b for nanostars before and after functionalization, respectively. In contrast to the ferret radius, the radius of curvature of the nanostar tips does not change significantly upon 6-MHA functionalization (it varies from 4.4 to 4.5 nm), so a Hamaker constant of 3.85×10^{-19} J can be used to model both samples. The total interaction pair potential and maximum potential barrier vary systematically as a function of ionic strength as shown in Fig. 5c. Several notable differences are apparent when these plots are compared with those obtained using the ferret radius. First, the overall V_{max} is smaller for these nanostructures (<40/k_BT vs. <100/k_BT) at all ionic strengths when the radius of curvature is considered rather than the ferret radius. Second, the functionalized gold nanostars exhibit larger energy barriers at all ionic strengths than the electrostatically stabilized nanostars. This is reasonable given the large steric potentials that arise from the SAM. Finally, ionic strengths of ~20 and ~32 mM are predicted to lead to unstable nanostars without and with SAM functionalization, respectively. These predictions are consistent with the results from LSPR. This implies that the smallest solution-phase nanostructure dimension dictates nanostructure stability, and this smallest dimension can be used to predict whether or not nanostructures will remain suspended in solution for a particular period of time.

All in all, DLVO modeling and collision theory provide a strong platform for understanding how the experimentally observed optical stability of gold nanostars varies in solution as a function of time and ionic strength. Using this approach, the stability of these nanostructures in solution can be predicted in advance of any analytical or bioanalytical application, which has previously not been possible for anisotropic nanostructures. This is important because nanostructures in solution will collide. The probability of cluster formation due to a collision depends on the kinetic energies of the particles as well as the potential energy landscapes at the particle surfaces. These depend on the nanostructure dimensions and can be predicted using collision theory and DLVO modeling, respectively. The use of the average nanoparticle size led to an overestimation of nanostar stability relative to experimental measurements. Instead, comparisons of the theoretical results with LSPR spectral data for gold nanostars as a function of ionic strength revealed that the smallest nanostructure dimension—the tips of the nanostar branches in this case—dictated solution-phase nanostructure stability. This discovery could be very useful for researchers who employ these materials in subsequent analytical and bioanalytical measurements.

Conclusions

In summary, the experimentally observed solution-phase gold nanostar stability before and after functionalization with 6-mercaptohexanoic acid can be predicted accurately using (extended) DLVO theory and collision theory if the radius of curvature of the nanostar tips is considered along with the surface potential and/or the SAM thickness. LSPR spectra of nanostars with and without functionalization provided experimental evidence of nanostar instability by revealing time-dependent changes in extinction maximum wavelength and relative integrated spectral area near 1000 nm. Experimental results were consistent with modeling predictions obtained by comparing the calculated minimum required kinetic energy of the nanostructures from collision theory with the maximum energy barrier of the nanostructures from DLVO theory as a function of ionic strength. Accurate predictions of experimental behavior were achieved when the smallest nanostructure dimension was considered. These results suggest that small changes in this dimension, which corresponds to a nanostructure region with high chemical potential, likely govern shelf-lives in solution and influence the use of these and other increasingly popular anisotropic nanostructures in various applications.

Acknowledgements We thank Dr. Grace Lu for performing initial measurements relating to these studies. This work was funded by the National Science Foundation (CHE-1707859; unfunctionalized materials) and the National Institute of Environmental Health Sciences of the National Institutes of Health under award number R01ES027145 (SAM-functionalized materials).

Author contributions All of the authors contributed to the writing of the manuscript and gave their approval to the final version of it.

Compliance with ethical standards

Conflict of interest The authors declare that they have no conflict of interest.

References

1. Wu H-L, Chen C-H, Huang MH. Seed-mediated synthesis of branched gold nanocrystals derived from the side growth of pentagonal bipyramids and the formation of gold nanostars. Chem Mater. 2008;21(1):110–4.
2. Barbosa S, Agrawal A, Rodríguez-Lorenzo L, Pastoriza-Santos I, Alvarez-Puebla RA, Kornowski A, et al. Tuning size and sensing properties in colloidal gold nanostars. Langmuir. 2010;26(18):14943–50.
3. Moukarzel W, Fitremann J, Marty J-D. Seed-less amino-sugar mediated synthesis of gold nanostars. Nano. 2011;3(8):3285–90.
4. Casu A, Cabrini E, Donà A, Falqui A, Diaz-Fernandez Y, Milanese C, et al. Controlled synthesis of gold nanostars by using a zwitterionic surfactant. Chem Eur J. 2012;18(30):9381–90.
5. Zou X, Ying E, Dong S. Seed-mediated synthesis of branched gold nanoparticles with the assistance of citrate and their surface-enhanced Raman scattering properties. Nanotechnology. 2006;17(18):4758.
6. Yuan H, Khoury CG, Hwang H, Wilson CM, Grant GA, Vo-Dinh T. Gold nanostars: surfactant-free synthesis, 3D modelling, and two-photon photoluminescence imaging. Nanotechnology. 2012;23(7):075102.
7. Chatterjee S, Ringane A, Arya A, Das G, Dantham V, Laha R, et al. A high-yield, one-step synthesis of surfactant-free gold nanostars and numerical study for single-molecule SERS application. J Nanopart Res. 2016;18(8):242.
8. Sheen Mers S, Umadevi S, Ganesh V. Controlled growth of gold nanostars: effect of spike length on SERS signal enhancement. ChemPhysChem. 2017;18(10):1358–69.
9. Bibikova O, Haas J, López-Lorente A, Popov A, Kinnunen M, Meglinski I, et al. Towards enhanced optical sensor performance: SEIRA and SERS with plasmonic nanostars. Analyst. 2017;142(6):951–8.
10. Li M, Kang JW, Dasari RR, Barman I. Shedding light on the extinction-enhancement duality in gold nanostar-enhanced Raman spectroscopy. Angew Chem Int Ed. 2014;53(51):14115–9.
11. Popov AP, Zvyagin AV, Lademann J, Roberts MS, Sanchez W, Priezzhev AV, et al. Designing inorganic light-protective skin nanotechnology products. J Biomed Nanotechnol. 2010;6(5):432–51.
12. Tian F, Conde J, Bao C, Chen Y, Curtin J, Cui D. Gold nanostars for efficient in vitro and in vivo real-time SERS detection and drug delivery via plasmonic-tunable Raman/FTIR imaging. Biomaterials. 2016;106:87–97.
13. Schütz M, Steinigeweg D, Salehi M, Kömpe K, Schlücker S. Hydrophilically stabilized gold nanostars as SERS labels for tissue imaging of the tumor suppressor p63 by immuno-SERS microscopy. Chem Commun. 2011;47(14):4216–8.
14. Vega MM, Bonifacio A, Lughi V, Marsi S, Carrato S, Sergo V. Long-term stability of surfactant-free gold nanostars. J Nanopart Res. 2014;16(11):1–6.
15. Zhao L, Ji X, Sun X, Li J, Yang W, Peng X. Formation and stability of gold nanoflowers by the seeding approach: the effect of intraparticle ripening. J Phys Chem C. 2009;113(38):16645–51.
16. Hojo M, Yamamoto M, Okamura K. Dilute nitric or nitrous acid solution containing halide ions as effective media for pure gold dissolution. PCCP. 2015;17(30):19948–56.
17. Rahman DS, Chatterjee H, Ghosh SK. Excess surface energy at the tips of gold nanospikes: from experiment to modeling. J Phys Chem C. 2015;119(25):14326–37.
18. Shiohara A, Langer J, Polavarapu L, Liz-Marzán LM. Solution processed polydimethylsiloxane/gold nanostar flexible substrates for plasmonic sensing. Nano. 2014;6(16):9817–23.
19. Chandra K, Culver KSB, Werner SE, Lee RC, Odom TW. Manipulating the anisotropic structure of gold nanostars using Good's buffers. Chem Mater. 2016;28(18):6763–9.
20. Yuan H, Fales AM, Khoury CG, Liu J, Vo-Dinh T. Spectral characterization and intracellular detection of surface-enhanced Raman scattering (SERS)-encoded plasmonic gold nanostars. J Raman Spectrosc. 2013;44(2):234–9.
21. Sun M, Liu F, Zhu Y, Wang W, Hu J, Liu J, et al. Salt-induced aggregation of gold nanoparticles for photoacoustic imaging and photothermal therapy of cancer. Nano. 2016;8(8):4452–7.
22. D'Agostino A, Taglietti A, Bassi B, Donà A, Pallavicini P. A naked eye aggregation assay for Pb^{2+} detection based on glutathione-coated gold nanostars. J Nanopart Res. 2014;16(10):2683.
23. Ramsey JD, Zhou L, Kyle Almlie C, Lange JD, Burrows SM. Achieving plasmon reproducibility from surfactant free gold nanostar synthesis. New J Chem. 2015;39(12):9098–108.
24. Stein B, Zopes D, Schmudde M, Schneider R, Mohsen A, Goroncy C, et al. Kinetics of aggregation and growth processes of PEG-stabilised mono-and multivalent gold nanoparticles in highly concentrated halide solutions. Faraday Discuss. 2015;181:85–102.
25. Rodríguez-Lorenzo L, Álvarez-Puebla RA, de Abajo FJG, Liz-Marzán LM. Surface enhanced Raman scattering using star-shaped gold colloidal nanoparticles. J Phys Chem C. 2010;114(16):7336–40.
26. Navarro JRG, Liotta A, Faure A-C, Lerouge F, Chaput F, Micouin G, et al. Tuning dye-to-particle interactions toward luminescent gold nanostars. Langmuir. 2013;29(34):10915–21.
27. Dey P, Blakey I, Thurecht KJ, Fredericks PM. Self-assembled hyperbranched polymer–gold nanoparticle hybrids: understanding the effect of polymer coverage on assembly size and SERS performance. Langmuir. 2013;29(2):525–33.
28. Cao G, Wang Y. Nanostructures and nanomaterials: synthesis, properties, and applications. Singapore: World Scientific; 2011.
29. Verwey EJ, Overbeek JTG. Theory of stability of lyophobic colloids. 1st ed. Amsterdam: Elsevier; 1948.
30. Derjaguin B. A theory of interaction of particles in presence of electric double layers and the stability of lyophobe colloids and disperse systems. Prog Surf Sci. 1993;43(1):1–14.
31. Derjaguin B, Landau L. Theory of the stability of strongly charged lyophobic sols and of the adhesion of strongly charged particles in solutions of electrolytes. Prog Surf Sci. 1993;43(1):30–59.
32. White LR. On the Deryaguin approximation for the interaction of macrobodies. J Colloid Interface Sci. 1983;95(1):286–8.
33. Cai J, Raghavan V, Bai YJ, Zhou MH, Liu XL, Liao CY, et al. Controllable synthesis of tetrapod gold nanocrystals with precisely tunable near-infrared plasmon resonance towards highly efficient surface enhanced Raman spectroscopy bioimaging. J Mater Chem B. 2015;3(37):7377–85.
34. Lu G, Forbes TZ, Haes AJ. SERS detection of uranyl using functionalized gold nanostars promoted by nanoparticle shape and size. Analyst. 2016;141(17):5137–43.
35. de Puig H, Tam JO, Yen C-W, Gehrke L, Hamad-Schifferli K. Extinction coefficient of gold nanostars. J Phys Chem C. 2015;119(30):17408–15.
36. Ohshima H. A simple expression for Henry's function for the retardation effect in electrophoresis of spherical colloidal particles. J Colloid Interface Sci. 1994;168(1):269–71.
37. Wijenayaka LA, Ivanov MR, Cheatum CM, Haes AJ. Improved parametrization for extended Derjaguin, Landau, Verwey, and Overbeek predictions of functionalized gold nanosphere stability. J Phys Chem C. 2015;119(18):10064–75.
38. Pinchuk AO. Size-dependent Hamaker constant for silver nanoparticles. J Phys Chem C. 2012;116(37):20099–102.
39. Lee K, Sathyagal AN, McCormick AV. A closer look at an aggregation model of the Stober process. Colloids Surf A. 1998;144(1–3):115–25.
40. Vincent B, Edwards J, Emmett S, Jones A. Depletion flocculation in dispersions of sterically-stabilised particles ("soft spheres"). Colloids Surf. 1986;18(2):261–81.

41. Skoglund S, Lowe TA, Hedberg J, Blomberg E, Wallinder IO, Wold S, et al. Effect of laundry surfactants on surface charge and colloidal stability of silver nanoparticles. Langmuir. 2013;29(28):8882–91.
42. Li A, Tang L, Song D, Song S, Ma W, Xu L, et al. A SERS-active sensor based on heterogeneous gold nanostar core-silver nanoparticle satellite assemblies for ultrasensitive detection of aflatoxin B1. Nano. 2016;8(4):1873–8.
43. Gołąbiewska A, Malankowska A, Jarek M, Lisowski W, Nowaczyk G, Jurga S, et al. The effect of gold shape and size on the properties and visible light-induced photoactivity of au-TiO_2. Appl Catal B Environ. 2016;196:27–40.
44. Leopold MC, Black JA, Bowden EF. Influence of gold topography on carboxylic acid terminated self-assembled monolayers. Langmuir. 2002;18(4):978–80.
45. Hill HD, Millstone JE, Banholzer MJ, Mirkin CA. The role radius of curvature plays in thiolated oligonucleotide loading on gold nanoparticles. ACS Nano. 2009;3(2):418–24.
46. Webb JA, Erwin WR, Zarick HF, Aufrecht J, Manning HW, Lang MJ, et al. Geometry-dependent plasmonic tunability and photothermal characteristics of multibranched gold nanoantennas. J Phys Chem C. 2014;118(7):3696–707.
47. Haes AJ, Van Duyne RP. A nanoscale optical biosensor: sensitivity and selectivity of an approach based on the localized surface plasmon resonance spectroscopy of triangular silver nanoparticles. J Am Chem Soc. 2002;124(35):10596–604.
48. Jung LS, Campbell CT, Chinowsky TM, Mar MN, Yee SS. Quantitative interpretation of the response of surface plasmon resonance sensors to adsorbed films. Langmuir. 1998;14(19):5636–48.
49. Sobral H, Peña-Gomar M. Determination of the refractive index of glucose-ethanol-water mixtures using spectroscopic refractometry near the critical angle. Appl Opt. 2015;54(28):8453–8.
50. Volkert AA, Pierre MCS, Shrestha B, Haes AJ. Implications of sample aging on the formation of internally etched silica coated gold nanoparticles. RSC Adv. 2015;5(5):3774–80.
51. Das K, Uppal A, Gupta PK. Hyper-Rayleigh scattering and continuum generation of salt induced aggregates of silver nanoparticles: the effect of cation size (Li^+, Na^+ and K^+). Chem Phys Lett. 2006;426(1):155–8.
52. Kim JH, Park JS, Kim MG. Time-dependent change of hyper-Rayleigh scattering from silver nanoparticle aggregates induced by salt. Chem Phys Lett. 2014;600(600):15–20.
53. Fraire JC, Pérez LA, Coronado EA. Cluster size effects in the surface-enhanced Raman scattering response of Ag and Au nanoparticle aggregates: experimental and theoretical insight. J Phys Chem C. 2013;117(44):23090–107.
54. Ivanov MR, Haes AJ. Anionic functionalized gold nanoparticle continuous full filling separations: importance of sample concentration. Anal Chem. 2012;84(3):1320–26.
55. Haiss W, Thanh NTK, Aveyard J, Fernig DG. Determination of size and concentration of gold nanoparticles from UV−Vis spectra. Anal Chem. 2007;79(11):4215–21.
56. Hostomsky J, Jones A. Calcium carbonate crystallization, agglomeration and form during continuous precipitation from solution. J Phys D Appl Phys. 1991;24(2):165.
57. Hotze EM, Phenrat T, Lowry GV. Nanoparticle aggregation: challenges to understanding transport and reactivity in the environment. J Environ Qual. 2010;39(6):1909–24.
58. Zhou J, Ralston J, Sedev R, Beattie DA. Functionalized gold nanoparticles: synthesis, structure and colloid stability. J Colloid Interface Sci. 2009;331(2):251–62.

Wenjing Xi earned both B.S. and M.S. degrees in Pharmaceutical Engineering from East China University of Science and Technology and is currently a Ph.D. candidate in the Chemistry Department at the University of Iowa under the direction of Prof. Amanda J. Haes. Her research focuses on improving the detectability of low concentrations of small molecules in complex samples using novel materials design and understanding how solution composition and molecular adsorption influences the magnitude and reproducibility of the SERS signal.

Hoa T. Phan earned a B.S. degree in Chemistry from Hanoi University of Science, Vietnam National University, and is currently a Ph.D. candidate in the Chemistry Department at the University of Iowa under the direction of Prof. Amanda J. Haes. His research focuses on investigating the influence of pH and molecular protonation on chemical enhancements using plasmonic materials stabilized in microporous silica membranes and improving the reproducibility in SERS detection of uranyl on flexible substrates.

Amanda J. Haes is Associate Professor in the Chemistry Department and Associate Director of the Nanoscience and Nanotechnology Institute at the University of Iowa. She focuses her research efforts on a number of key issues related to nanoscience and nanotechnology including understanding nanomaterial design, measuring and modeling how intermolecular forces influence interfacial phenomena in plasmonics and SERS, as well as applying these materials in biological, chemical, dental, environmental, and radiological applications.